Breaking crystalline symmetry of epitaxial SnTe films by strain

Steffen Schreyeck,* Karl Brunner, and Laurens W. Molenkamp
Institute for Topological Insulators and Physikalisches Institut, Experimentelle Physik III, Universität Würzburg, Am Hubland, 97074 Würzburg, Germany

Grzegorz Karczewski
Institute of Physics, Polish Academy of Sciences, Aleja Lotników 32/46, 02-668 Warsaw, Poland

Martin Schmitt,† Paolo Sessi, Matthias Vogt, Stefan Wilfert, Artem B. Odobesko, and Matthias Bode
Physikalisches Institut, Experimentelle Physik II, Universität Würzburg, Am Hubland, 97074 Würzburg, Germany

(Received 30 November 2018; published 12 February 2019)

SnTe belongs to the recently discovered class of topological crystalline insulators. Here, we study the formation of line defects which break crystalline symmetry by strain in thin SnTe films. Strained SnTe(111) films are grown by molecular beam epitaxy on lattice and thermal expansion coefficient-mismatched CdTe. To analyze the structural properties of the SnTe films, we applied *in situ* reflection high-energy electron diffraction, x-ray reflectometry, high-resolution x-ray diffraction, reciprocal space mapping, and scanning tunneling microscopy. This comprehensive analytical approach reveals a twinned structure, tensile strain, bilayer surface steps, and dislocation line defects forming a highly ordered dislocation network for thick films with local strains up to 31% breaking the translational crystal symmetry.

DOI: 10.1103/PhysRevMaterials.3.024203

I. INTRODUCTION

The recently discovered new material class of topological insulators attracted a lot of interest in condensed-matter physics [1–3]. Fu extended the topological classification of band structures by including crystal point-group symmetries, i.e., the theoretical prediction of topological crystalline insulators (TCIs) [4]. In contrast to topological insulator materials where the surface states are protected by time-reversal symmetry, the surface states of TCIs are protected by the crystal symmetry, resulting in an insulating bulk and metallic surface states on high-symmetry crystal surfaces, such as (001) and (111) planes [5]. The first experimentally discovered TCIs belong to the cubic rocksalt family, namely, the lead tin salts $Pb_{1-x}Sn_xSe$ for $x \geqslant 0.2$, SnTe, and $Pb_{1-x}Sn_xTe$ for $x \geqslant 0.4$ [6–8]. For the latter, the spin-polarized nature of the Dirac surface states has been observed by spin-resolved angle-resolved photoemission spectroscopy measurements [8]. The reduction of crystal symmetry opens the possibility to establish energy shifts or band gaps [9,10]. Sessi *et al.* showed that breaking the translational symmetry at odd surface steps on cleaved $Pb_{1-x}Sn_xSe(001)$ bulk crystals results in topological one-dimensional edge states [11]. Such line defects may allow for the creation of well-separated conductive channels, which can be patterned and contacted in thin TCI films for spintronics devices [11].

We investigate molecular beam epitaxy (MBE) of rocksalt TCI thin films to control the crystal orientation and the formation of crystalline line defects at the surface. The IV–VI rocksalt structure is known to build a glide plane system under epitaxial and thermal strains forming dislocations at the interface to the substrate, which extend to the surface [12–14]. The MBE growth of SnTe has been studied on various substrates, including Si, BaF_2, Bi_2Te_3, PbSe, and CdTe [15–19]. Here, we study epitaxy of thin SnTe(111) films, a facet that is hardly accessible by crystal cleaving [20], on lattice mismatched CdTe(111) to obtain in-plane tensile strain. For strain analysis, we grow films in the thickness range from 8.5 to 425 nm on CdTe. SnTe crystallizes in a rocksalt structure with a room-temperature lattice mismatch of 2.6% to the cubic zinc-blende lattice of CdTe. In addition, the linear thermal expansion coefficient of SnTe (2×10^{-5}/K) is about a factor of 3 larger than that of CdTe (6×10^{-6}/K) introducing additional in-plane tensile strain at low temperatures [21]. To study the structural quality and strain in the layers, we apply *in situ* reflection high-energy electron diffraction (RHEED), x-ray reflectometry (XRR), high-resolution x-ray diffraction (HRXRD), and HRXRD reciprocal space mapping (RSM). The structural properties of the pristine SnTe(111) surface are compared to the dislocation network by means of scanning tunneling microscopy (STM) at low temperatures.

II. EXPERIMENT

The SnTe films are grown by molecular beam epitaxy under ultrahigh-vacuum (UHV) conditions at a base pressure below 1×10^{-10} mbar. As a virtual substrate, we use a several-micrometer-thick CdTe buffer layer, which is grown on a 2-in. Si-doped *n*-type GaAs(111)B wafer (B implies As-terminated surface). In between the buffer and the wafer,

*sschreyeck@physik.uni-wuerzburg.de
†maschmitt@physik.uni-wuerzburg.de

 ©2019 American Physical Society

a 6-nm-thin ZnTe film is deposited to reduce the lattice mismatch of about 13% and to enable CdTe(111) growth [22]. After the buffer growth, this substrate is divided into about 1×0.5 cm^2-sized pieces suitable for STM experiments. This *ex situ* procedure assures that all future experiments will be performed on substrates with comparable quality. The individual substrate pieces are etched by 12% aqueous HCl solution for 30 s to remove the oxide layer before they are indium glued on an UHV sample holder. The holders are equipped with a movable tantalum spring for providing electrical top contact to the sample surface after growth allowing further STM characterization.

After reintroduction into the MBE chamber, the RHEED pattern of the etched CdTe surface shows a mixture of amorphous and polycrystalline features, which is caused by nearly unordered elemental Te remaining on the CdTe buffer layer after *ex situ* HCl etching. To restore the surface quality, the substrates are first heated to the CdTe buffer growth temperature of 300 °C thereby desorbing excess Te as confirmed by a change in the RHEED pattern from diffuse and spotty to a streaky pattern. After Te desorption, the bare CdTe surface is protected by applying Te flux and an additional 0.5-μm CdTe layer is grown on the CdTe(111) buffer to renew the surface. Most parts of this layer are grown at 300 °C, but the sample is cooled to the SnTe growth temperature of 260 °C towards the end of CdTe growth when a Cd-rich surface is prepared by closing the Te shutter applying only the Cd flux. Immediately after closing the Cd shutter, the SnTe growth is initiated by co-deposition of Sn and Te. The applied elemental fluxes of Sn and Te have constant beam equivalent pressures of 9×10^{-7} and 9×10^{-6} mbar, respectively. Beam equivalent pressures are measured by an ionization gauge (after Bayard-Alpert) and are corrected by ionization sensitivity, source temperature, and masses of the impinging particles. The structural properties of the SnTe films are analyzed by *in situ* RHEED and an *ex situ* Panalytical Xper't materials research diffractometer HRXRD equipped with a Cu $K\alpha 1$ source after the In-glued samples were removed from the sample holders at a temperature of about 180 °C. The SnTe layers investigated in this paper were grown for 250, 500, 2500, and 12 500 s to obtain a series with different film thicknesses.

After the growth, a tantalum spring is positioned *in situ* on top of the SnTe film by a wobble stick to ensure a proper electrical grounding for STM measurements. Afterwards, the samples are transferred into an UHV-suitcase and transported to the STM setup at a base pressure below 5×10^{-10} mbar. Scanning probe experiments are carried out in a homebuilt low-temperature scanning tunneling microscope operating at a temperature of $T \approx 5.5$ K. All topographic images are obtained in constant-current mode with tungsten tips.

III. RESULTS AND DISCUSSION

A. Epitaxy

The CdTe buffer growth on the GaAs(111)B substrate is monitored by RHEED. Although the streaky RHEED pattern of the *in situ* grown CdTe indicates a two-dimensional (2D) growth mode, the second layer after *ex situ* etching shows streaks and spots (data not shown here). Whereas the sharp streaks confirm the presence of atomically flat areas on the CdTe buffer, the spots result from a partially rough surface after *ex situ* preparation. The symmetrical alignment of the spots indicates a twinned CdTe layer structure. Subsequently, the growth of the SnTe on the CdTe buffer results in a decreasing intensity of the spots and increasing intensity of the streaks in the RHEED pattern. After a few nanometers of SnTe, the spots vanish, and a streaky RHEED pattern of a (1×1)-ordered hexagonal surface with distinct Kikuchi lines remains indicating a predominant 2D growth mode at the surface as shown in Fig. 1(a).

B. Bulk crystal structure and strain

XRR measurements are conducted to determine the layer thickness of the SnTe films. Figure 1(b) shows a XRR curve with distinct fringes resulting in a SnTe film thickness of 17 ± 2 nm. The layer thicknesses of the SnTe series are 8.5, 17, 85, and 425 nm as extrapolated from the XRR thickness measurement versus the growth time, resulting in a growth rate of 0.34 Å s^{-1}.

The large-scale θ-2θ HRXRD measurements reveal exclusively the 1 1 1, 2 2 2, and 3 3 3 reflections of GaAs, CdTe, and SnTe as shown in Fig. 1(c), confirming the parallel alignment of the GaAs, CdTe, and SnTe(111) surface planes as well as indicating the absence of other crystalline phases and orientations. Pole scans in Fig. 1(d) of the asymmetric reflections of the {400} planes display the expected threefold symmetry of the GaAs(111) substrate. In contrast, the CdTe buffer and the SnTe reflections show two peak triplets resulting in a sixfold symmetry thereby confirming the presence of twinned domains rotated by 180° to each other. One of the peak triplets, labeled T1 in Fig. 1(c), is located at the same in-plane rotation angle as the GaAs and CdTe reflections confirming parallel orientation of the {400} planes of the twin T1 with that of the substrate and the buffer. This indicates a well-aligned crystalline interface between the rocksalt and the zinc-blende crystal structures. The comparable peak intensities of triplets T1 and T2 suggest a nearly equal twin distribution for SnTe, which also applies for the CdTe buffer. The formation of twin domains is a well-known crystal defect in epitaxial CdTe on (111) substrates and is attributed to the presence of domains with different stacking orders, i.e., ABC and ACB [23].

HRXRD RSMs are used to study the strain within the layers at room temperature after cooling the samples from growth temperature to 5.5 K and heating them to about 453 K to remove the In-glued substrate holder. Note that the thermal treatment of the sample, which is an unavoidable need towards our STM investigation, significantly impacts the formation of defects and strain as will be discussed later in Sec. III D. The 4 2 2 reflections of buffer and film, which are both accessible in ω-plus and ω-minus geometry {2θ-ω diffractogram with $\omega = \theta \pm \angle([111],[422])$}, are investigated. The angle between the [111] and [422] directions is 19.47° in a cubic relaxed zinc-blende or rocksalt structure. The RSMs of the 17-, 85-, and 425-nm films are plotted in Figs. 2(a)–2(c). They show an intense 4 2 2 reflection of the CdTe buffer appearing under an angle of 19.49° to the [111] direction, slightly above the expected value, indicating that the CdTe is nearly completely relaxed. With increasing layer thickness,

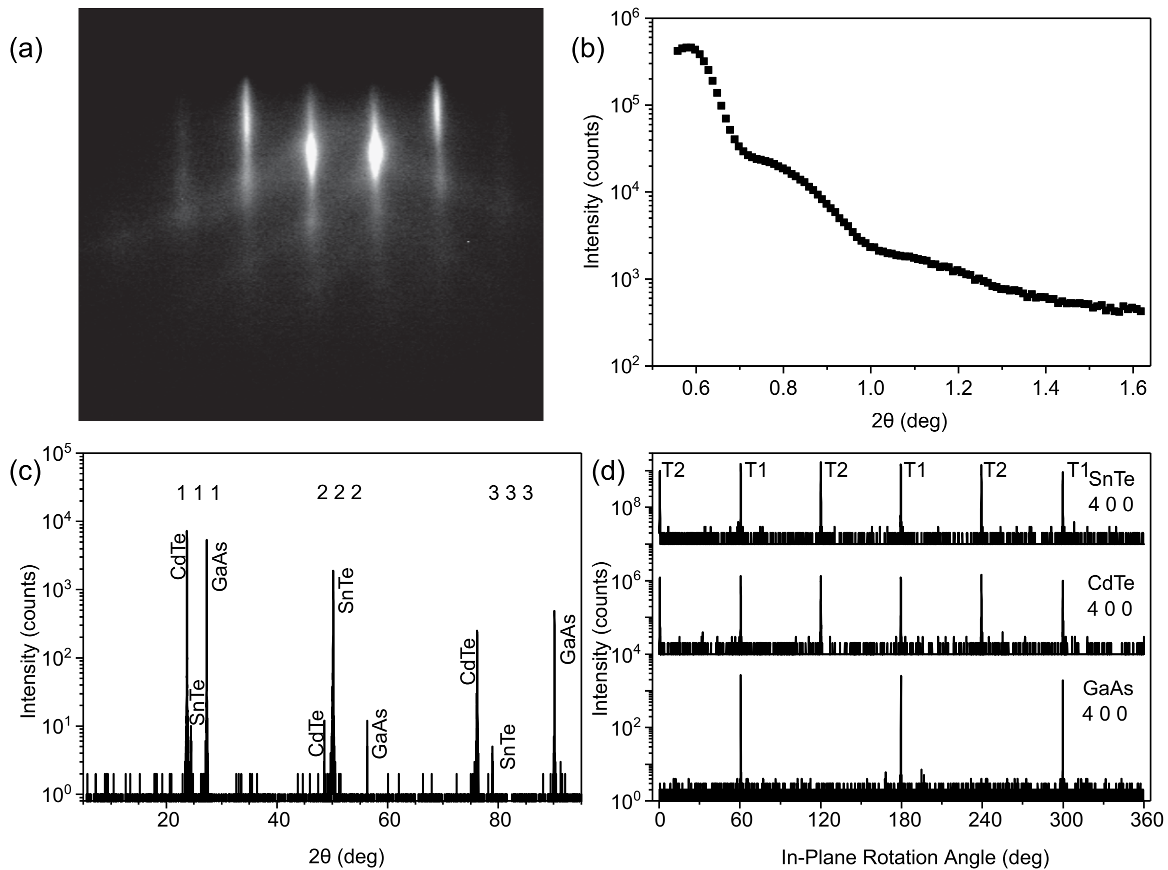

FIG. 1. (a) Representative RHEED image taken after 170-nm SnTe MBE growth. (b) XRR measurement of a thin SnTe film to determine the SnTe layer thickness, i.e., 17 nm. (c) Large overview HRXRD θ-2θ diffractogram of the 425-nm-thick SnTe sample displaying the 1 1 1, 2 2 2, and 3 3 3 reflections of GaAs, CdTe, and SnTe. (d) HRXRD pole scans of the asymmetric 4 0 0 reflections of the 425-nm-thick SnTe sample. The two triplets of twin reflections are labeled T1 and T2.

the intensity of the SnTe 4 2 2 reflections increases, and their width in ω and 2θ decreases. The angle between the [111] direction and the measured 4 2 2 reflection of SnTe, $\alpha = 19.36^\circ$ for the 425-nm film, is significantly below the calculated value in a relaxed crystal, indicating a distortion of the cubic rocksalt structure.

This distortion is analyzed in more detail by comparing the in-plane and out-of-plane lattice constants of the strained SnTe relative to that of the relaxed CdTe buffer. Therefore, the difference of the $Q_\parallel$ and $Q_\perp$ positions of the 4 2 2 reflections are determined. The relative differences among lattice constants of the CdTe buffer and the SnTe layers are 2.23%, 2.20%, and 2.15% within the film plane and 2.71%, 2.86%, and 2.99% normal to the film plane for the 17-, 85-, and 425-nm films, respectively. The deviation from the expected literature value of 2.6% mismatch is plotted in Fig. 2(d). The in-plane strain is tensile, and the out-of-plane strain is compressive as expected for the growth on the larger lattice of CdTe. Surprisingly, these values indicate an increase in strain with increasing layer thickness. We assume the unexpected increase in strain with thickness is either related to an enhanced relaxation of thin films due to island growth or related to the thermal expansion coefficient mismatch between SnTe and CdTe of about a factor of 3. The thermal mismatch combined with the thermal treatment of the samples before the HRXRD analysis, i.e., the cooling from 260 °C (533-K) growth temperature to 5.5-K for STM measurements and successive warming to ambient conditions, may cause this uncommon strain behavior in these films [13].

C. Topography and surface structure

To investigate the structural properties of the SnTe(111) surface and the consequences of the in-plane strain, we performed STM measurements on all four samples with film thicknesses ranging from 8.5 nm up to 425 nm at low temperatures of $T = 5.5$ K. In the case of the 8.5-nm film, it was found to be electrically insulating, making it inaccessible by STM. We found two plausible explanations for this behavior. First, a hybridization of surface states located at the top and bottom of the film could open a band gap resulting in an insulating SnTe film. Second, an inhomogeneous coverage of the substrate could lead to a discontinuous film with insufficient electrical grounding through the tantalum spring.

As shown in Fig. 3, the thicker SnTe(111) films could be imaged by STM. The topography of the 17-nm-thick film as depicted in Fig. 3(a) is atomically flat and slightly buckled. Besides local pointlike defects, we can also recognize dark lines which are oriented along the $\langle 1\bar{1}0\rangle$ directions and probably represent distinct dislocation lines. We also observe these dislocation lines for the 85-nm film in Fig. 3(b) and—most strikingly—they become even more abundant for the

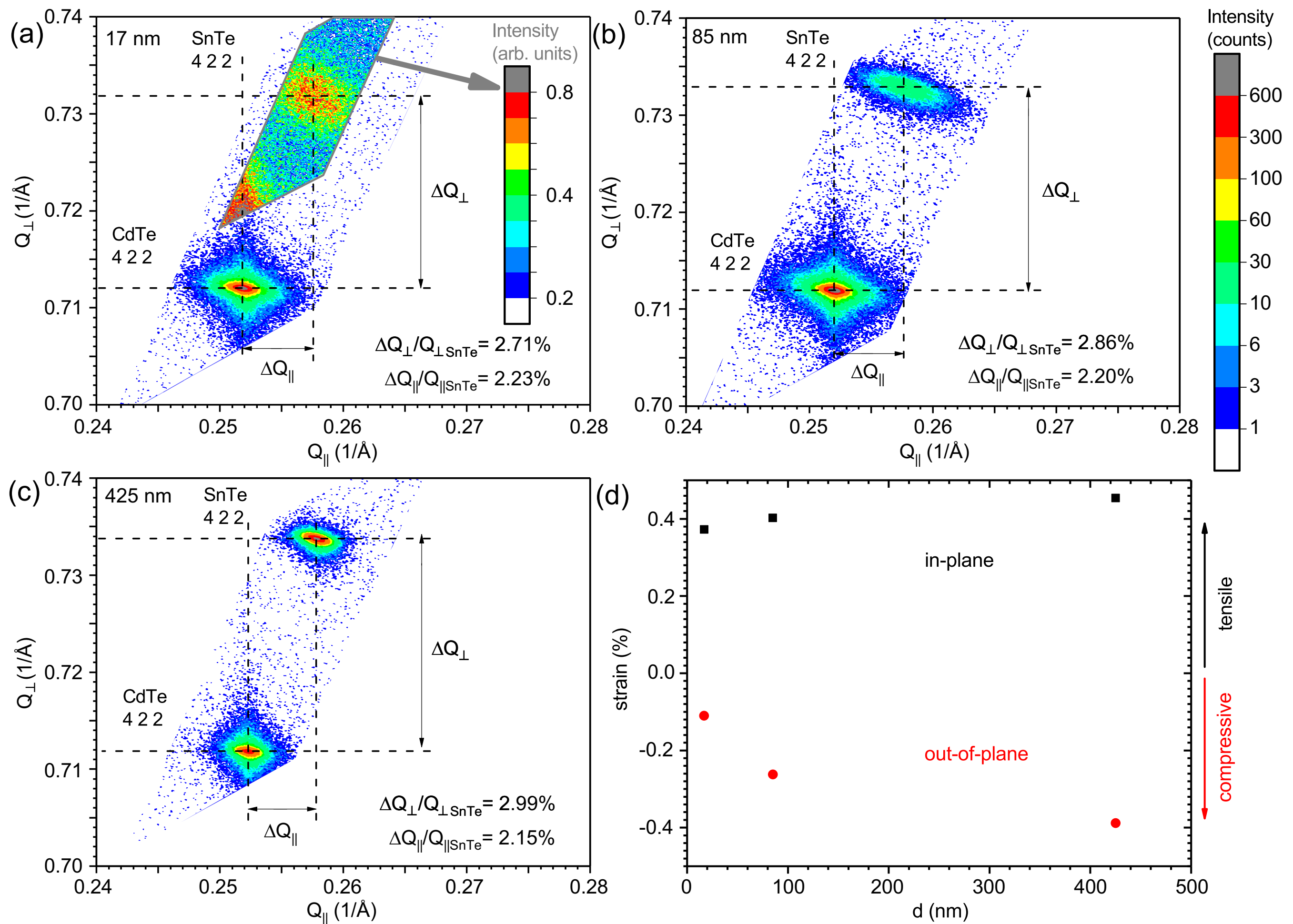

FIG. 2. Reciprocal space maps of the CdTe and SnTe 4 2 2 reflections of samples with (a) 17 nm (b) 85 nm, and (c) 425 nm with the intensity scale in the upper right part. Note the inset in the gray frame in (a) of the SnTe reflection is measured with 30 times higher integration time and has, therefore, an other intensity scale. (d) Strain of SnTe determined by the relative deviation from the CdTe 4 2 2 reflection position in dependence of the film thickness.

425-nm film shown in Fig. 3(c) where periodic dislocation lines along $\langle 1\bar{1}0\rangle$ show up. This finding indicates that strain and relaxation process of SnTe films grown on CdTe comes along with a thickness-dependent dislocation line network, which may increase strain with increasing layer thickness during thermal treatment, as observed by HRXRD above in Sec. III A.

In the following, we will focus on 425-nm-thick films which exhibit periodic dislocation lines with a length of up to several hundreds of nanometers and occasional well-separated atomic scale defects. Our investigations revealed that the structural properties of both point and line defects of these rather thick films are representative also for thinner SnTe films on CdTe with the only difference being the density of the particular defects.

The large overview STM scan of a 425-nm film in Fig. 4(a) is typical for those films and comparable to the work of Ishikawa *et al.*, who optimized the growth parameters of SnTe on CdTe substrates [19]. The surface is covered by large mesas, i.e., relatively flat areas often exhibiting extended atomically flat terraces, which are separated by steep cliffs forming up to 15-nm-deep trenches. Close inspection shows that these cliffs are not abrupt but consist of a dense sequence of steps with step heights that are equivalent to single bilayers. As sketched by the blue triangles in Fig. 4(a), the cliffs surrounding the mesas as well as the few step edges on their tops are oriented along the $\langle 1\bar{1}0\rangle$ directions whereby the orientation of the triangles rotate by 180° between neighboring mesas. This result is consistent with the existence of twin domains with different stacking orders [24] as already obtained from the HRXRD pole scans displayed in Fig. 1(d).

In addition to the occasional step edges oriented in the $\langle 1\bar{1}0\rangle$ directions, we observe wide areas with parallel periodically arranged dislocation lines on top of the mesas as depicted in Fig. 4(b). These lines are directed in the very same high-symmetry directions as the step edges. Their mean separation can be obtained from the Fourier transformation of the STM image, which is displayed as an inset on the top right of Fig. 4(b). An analysis of the separation of the two outer spots from the central spot located at zero reciprocal length results in a periodicity of (8 ± 1) nm. Furthermore, we can recognize dark and bright areas with ridges along the $[11\bar{2}]$ direction which are caused by a surface which is buckled on a

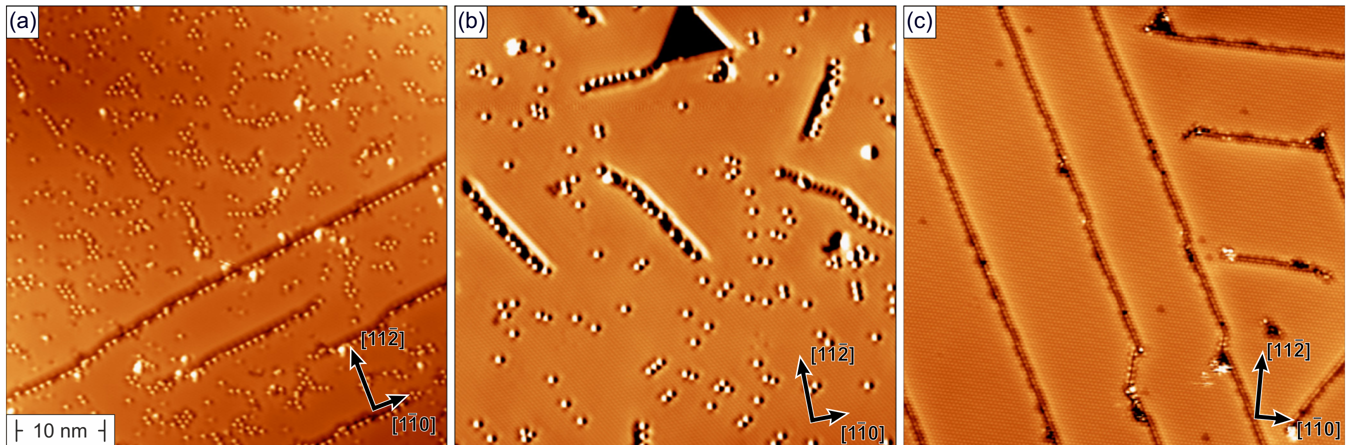

FIG. 3. Representative STM topographic images (50×50 nm^2) of SnTe(111) films with thicknesses of (a) 17 nm, (b) 85 nm, and (c) 425 nm. In each case, an area without step edges but occasional adatoms (white dots) and dislocation lines (dark lines) is shown. Whereas the adatom density decreases with film thickness, the number of dislocation lines appears to increase and even form a dislocation network. Scan parameters: (a) $U = 1$ V, $I = 300$ pA; (b) $U = 0.5$ V, $I = 500$ pA; (c) $U = 0.8$ V, $I = 300$ pA.

lateral scale of about 100 nm, also indicating the presence of strain in the film.

Figure 4(c) shows an STM image of a surface area with a step edge. The height profile measured along the blue line is shown in the central panel. In the lower panel, a sketch of the side and top views is sketched. Due to the fcc stacking, a natural breaking of the translational symmetry exists, which could potentially lead to a topological edge state, similar to what has been observed for $Pb_xSn_{(1-x)}Se(001)$ surfaces obtained by cleaving [11]. The step height amounts to $h = (3.75 \pm 0.25)$ Å, corresponding well to the literature value for a bilayer step edge between two Te (Sn) layers of 3.64 Å. This indicates that the (111) surface is either exclusively Te or Sn terminated. Otherwise, step edges with a height of half this value would be expected. Such step edges which would correspond to a transition from a Sn- to a Te-terminated terrace (or vice versa) have never been observed in these films. Theoretical investigations of the stability of the SnTe(111) surface predict three energetically stable surface structures [25]. The (1×1)-ordered Te surface for Te-rich growth, a $(\sqrt{3} \times \sqrt{3})$R30°-reconstructed surface at higher tin partial pressure, and a (2×1) Sn reconstruction for tin-rich growth. Based on the fact that we grow our samples in Te-rich conditions, together with the theoretical predictions of the stability of the SnTe(111) surface and the observed (1×1) streaks by RHEED, we conclude that we see a Te-terminated surface.

This assumption is also supported by the higher-resolution STM scan shown in Fig. 4(d). We see five dislocation lines oriented along the [1$\bar{1}$0] direction. In between these line defects, we observed a hexagonal lattice with a lattice constant of (4.72 ± 0.30) Å. This is in agreement with a (1×1)-ordered surface as determined by RHEED. Besides that, we only observe very few point defects, the most frequent types of which are exemplarily marked by black circles. Higher-resolution scans of these defects are shown in Fig. 4(e). They have typical appearances similar to other TI surfaces and can be found at all studied film thicknesses [26]. Defects (I)–(III) have the defect center in a threefold coordinated hollow site between the atoms of the top Te layer. Since defect (I) exhibits an about 0.81-Å-high protrusion in its center, we assign it to an adatom, probably Te. In contrast, the corrugation of defects (II) and (III) is much smaller. On the basis of the dimensions and their locations, we attribute the triangular defects to Sn vacancies in the second and the fourth layers, respectively. These kinds of defects have a negative formation energy and can be expected for Sn-poor growth [27]. The relatively rare defect IV appears as a 0.25-Å-deep depression centered at a position of the surface lattice. Therefore, we assign defect IV to a Te vacancy, although we cannot strictly rule out that it is caused by an impurity atom on a Te site.

D. Discussion of line defects

In the following, we want to discuss possible scenarios for the formation of the dislocation line defects. First, they could act as domain boundaries between regions with different stacking sites, e.g., *A* and *B*. This would cause an abrupt lateral shift of the atomic rows of 2.6 Å by crossing the defect line in Fig. 4(f). Here, the atoms in close proximity to the dislocation are displaced perpendicular to the line defect by 31%, i.e, 1.2 Å, probably to cope with the misfit strain between SnTe and CdTe as indicated by the line profile across the line defect. A closer inspection of the overview scans in Figs. 4(b) and 4(c) reveals that the dislocation lines are not infinitely long but terminate at specific locations and merge to one domain with the same stacking positions. The second scenario is a periodic dislocation patterning process in which lattice planes are added to or removed from the ends of dislocations. However, in contrast to compressively strained rocksalt (001) films, we observe no additional or missing planes at the ends of the dislocation lines [28]. Third, the rocksalt (111) films are known to form dislocations under compressive strain with their threading ends moving back and forth in the ⟨1$\bar{1}$0⟩ surface directions along the {001} planes of the bulk thereby forming a ⟨1$\bar{1}$0⟩ {001} glide system during thermal cycling [13]. We also observe dislocation lines oriented in the ⟨1$\bar{1}$0⟩ directions. In contrast to Zogg and Teodoropol [13],

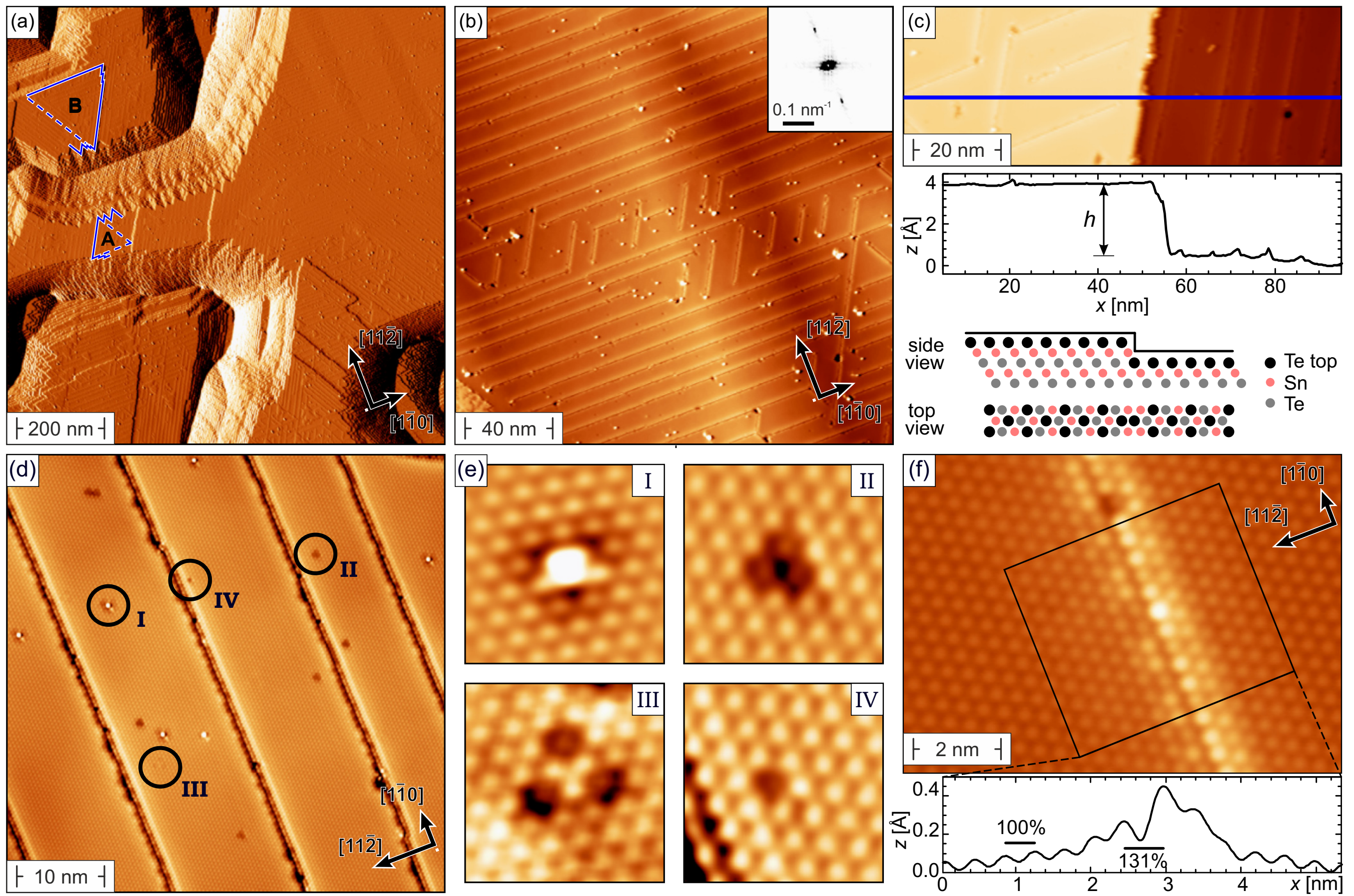

FIG. 4. (a) Overview STM scan of the 425-nm-thick SnTe(111) film on CdTe. Mesas with heights of several nanometers and triangular-shaped edges, indicated in blue, can be recognized. (b) Higher-resolution scan of the dislocation network on an extended area without step edges but numerous periodically arranged dislocation lines oriented along the $\langle 1\bar{1}0\rangle$ directions. The inset: Fourier transform of the image in (b). Analysis of the spot separation results in a dislocation line periodicity of (8 ± 1) nm. (c) STM image of a surface area with a step edge. The line profile shows a step height of $h = (3.75 \pm 25)$ Å. The sketch shows in the side view and the top view the broken translation symmetry at the step edges. (d) Large-scale atomic resolution scan showing four typical surface defects (I–IV). (e) Closeups of defects I–IV marked in (d). (f) Averaged height profile of atomic resolution data perpendicular to a dislocation line (black rectangle) indicates lateral translation of atomic rows perpendicular to the dislocation by 31%. Scan parameters: (a)–(c) $U = 2$ V, $I = 50$ pA; (d) and (e) $U = -0.8$ V, $I = 300$ pA; (f) $U = +0.8$ V, $I = 400$ pA.

the in-plane strain in our system is tensile, and the lattice mismatch is lower by a factor of 3. Therefore, we observe a locally increased lattice constant of up to 31% breaking the translational symmetry as shown in Fig. 4(f), perpendicular to the dislocation lines due to the tensile strain introduced by the CdTe. Whereas, first-principles calculations on SnTe indicate a closing of the gap and a topological phase transition to trivial band order already at 3% of tensile strain [7]. This suggests that a topological phase transition is likely to take place at the dislocation lines observed by STM. The mean increase in the in-plane lattice, measured perpendicular to dislocation lines, is 0.82 ± 0.14 Å distributed over several atomic positions. This corresponds to a mean elastic strain relaxation of 1.0% in the $\langle 11\bar{2}\rangle$ direction for the observed averaged periodical separation of dislocations, i.e., 8 nm, at a temperature of 5.5 K. The observed mean strain relaxation of about 1.0% is comparable to the expected thermal mismatch formed during cooling the sample from growth temperature to 5.5 K [29]. Therefore, SnTe appears to grow nearly relaxed forming a misfit dislocation network of 8-nm period at the interface to the CdTe buffer to overcome the lattice mismatch, and the strain measured by XRD is built up due to the thermal expansion coefficient mismatch between layer and buffer. The thermal cycling of the thin films with low dislocation densities results in threading ends moving back and forth to relax the thermal strain [13]. Whereas the films with higher dislocation densities and layer thicknesses have an increased probability of interaction and pinning of dislocations resulting in higher residual strain as shown by HRXRD reciprocal space maps at room temperature [13]. Therefore, we expect the tensile strain relaxation at glide planes to be the most likely explanation for the line defect formation since it can also describe the uncommon strain behavior in our films.

IV. CONCLUSION

To summarize, we present a study of strained topological crystalline insulator SnTe(111) thin films grown by MBE on

CdTe, a surface which is hardly accessible by *in situ* crystal cleaving. The structural analysis by HRXRD reciprocal space maps of these films gives insight into an uncommon strain relaxation mechanism resulting in residual strain increasing with layer thickness. We address this behavior to the formation and pinning of dislocations during the cooling procedure after growth due to the thermal expansion coefficients mismatch. STM measurements reveal bilayer surface steps and a network of highly ordered dislocation lines on the surface along the $\langle 1\bar{1}0 \rangle$ directions. Local strains up to 31% breaking the translational crystal symmetry are measured perpendicular to the several-hundreds-of-nanometers-long dislocation lines. These compensate the thermal expansion and lattice mismatch between SnTe and CdTe and form together with surface steps a playground for the study of topological surface states of this topological crystalline insulator with broken translational symmetry.

ACKNOWLEDGMENTS

We gratefully acknowledge financial support from the National Science Centre (Poland) through Grant No. UMO-2017/25/B/ST3/02966, and the DFG through the SFB 1170 ToCoTronics (Projects No. A02 and No. A05) and the Gottfried Wilhelm Leibniz Program.

S.S. and M.S. contributed equally to this work.

[1] C. L. Kane and E. J. Mele, Phys. Rev. Lett. **95**, 146802 (2005).
[2] B. A. Bernevig, T. L. Hughes, and S.-C. Zhang, Science **314**, 1757 (2006).
[3] M. Koenig, S. Wiedmann, C. Bruene, A. Roth, H. Buhmann, L. W. Molenkamp, X.-L. Qi, and S.-C. Zhang, Science **318**, 766 (2007).
[4] L. Fu, Phys. Rev. Lett. **106**, 106802 (2011).
[5] S.-Y. Xu, C. Liu, N. Alidoust, M. Neupane, D. Qian, I. Belopolski, J. Denlinger, Y. Wang, H. Lin, L. Wray, G. Landolt, B. Slomski, J. Dil, A. Marcinkova, E. Morosan, Q. Gibson, R. Sankar, F. Chou, R. Cava, A. Bansil, and M. Hasan, Nat. Commun. **3**, 1192 (2012).
[6] P. Dziawa, B. J. Kowalski, K. Dybko, R. Buczko, A. Szczerbakow, M. Szot, E. Lusakowska, T. Balasubramanian, B. M. Wojek, M. H. Berntsen, O. Tjernberg, and T. Story, Nature Mater. **11**, 1023 (2012).
[7] T. H. Hsieh, H. Lin, J. Liu, W. Duan, A. Bansil, and L. Fu, Nat. Commun. **3**, 982 (2012).
[8] Y. Tanaka, Z. Ren, T. Sato, K. Nakayama, S. Souma, T. Takahashi, K. Segawa, and Y. Ando, Nat. Phys. **8**, 800 (2012).
[9] P. Barone, D. Di Sante, and S. Picozzi, Phys. Status Solidi RRL **7**, 1102 (2013).
[10] L. Zhao, J. Wang, B.-L. Gu, and W. Duan, Phys. Rev. B **91**, 195320 (2015).
[11] P. Sessi, D. Di Sante, A. Szczerbakow, F. Glott, S. Wilfert, H. Schmidt, T. Bathon, P. Dziawa, M. Greiter, T. Neupert, G. Sangiovanni, T. Story, R. Thomale, and M. Bode, Science **354**, 1269 (2016).
[12] G. Bauer, Surf. Sci. **168**, 462 (1986).
[13] H. Zogg and S. Teodoropol, J. Cryst. Growth **150**, 1186 (1995).
[14] G. Springholz and G. Bauer, Phys. Status Solidi B **244**, 2752 (2007).
[15] C.-H. Yan, H. Guo, J. Wen, Z.-D. Zhang, L.-L. Wang, K. He, X.-C. Ma, S.-H. Ji, X. Chen, and Q.-K. Xue, Surf. Sci. **621**, 104 (2014).
[16] R. Akiyama, K. Fujisawa, T. Yamaguchi, R. Ishikawa, and S. Kuroda, Nano Res. **9**, 490 (2016).
[17] A. A. Taskin, F. Yang, S. Sasaki, K. Segawa, and Y. Ando, Phys. Rev. B **89**, 121302 (2014).
[18] I. Zeljkovic, D. Walkup, B. A. Assaf, K. L. Scipioni, R. Sankar, F. Chou, and V. Madhavan, Nat. Nanotechnol. **10**, 849 (2015).
[19] R. Ishikawa, T. Yamaguchi, Y. Ohtaki, R. Akiyama, and S. Kuroda, J. Cryst. Growth **453**, 124 (2016).
[20] Y. Tanaka, T. Shoman, K. Nakayama, S. Souma, T. Sato, T. Takahashi, M. Novak, K. Segawa, and Y. Ando, Phys. Rev. B **88**, 235126 (2013).
[21] G. Springholz, in *Lead Chalcogenides: Physics and Applications*, edited by D. Khokhlov, Optoelectronic Properties of Semiconductors and Superlattices Vol. 18 (Taylor & Francis, New York, 2003).
[22] M. Grynberg, S. Huant, G. Martinez, J. Kossut, T. Wojtowicz, G. Karczewski, J. M. Shi, F. M. Peeters, and J. T. Devreese, Phys. Rev. B **54**, 1467 (1996).
[23] Y. P. Chen, J. P. Faurie, S. Sivananthan, G. C. Hua, and N. Otsuka, J. Electron. Mater. **24**, 475 (1995).
[24] N. V. Tarakina, S. Schreyeck, M. Luysberg, S. Grauer, C. Schumacher, G. Karczewski, K. Brunner, C. Gould, H. Buhmann, R. E. Dunin-Borkowski, and L. W. Molenkamp, Adv. Mater. Interfaces **1**, 1400134 (2014).
[25] J. Wang, J. Liu, Y. Xu, J. Wu, B.-L. Gu, and W. Duan, Phys. Rev. B **89**, 125308 (2014).
[26] Y. Jiang, Y. Y. Sun, M. Chen, Y. Wang, Z. Li, C. Song, K. He, L. Wang, X. Chen, Q.-K. Xue, X. Ma, and S. B. Zhang, Phys. Rev. Lett. **108**, 066809 (2012).
[27] N. Wang, D. West, J. Liu, J. Li, Q. Yan, B.-L. Gu, S. B. Zhang, and W. Duan, Phys. Rev. B **89**, 045142 (2014).
[28] G. Springholz and K. Wiesauer, Phys. Rev. Lett. **88**, 015507 (2001).
[29] K. R. Knox, E. S. Bozin, C. D. Malliakas, M. G. Kanatzidis, and S. J. L. Billinge, Phys. Rev. B **89**, 014102 (2014).